Springer

KSME

Journal of Mechanical Science and Technology 25 (11) (2011) 2795~2803
www.springerlink.com/content/1738-494x
DOI 10.1007/s12206-011-0908-8

Gap-flow patterns behind twin-cylinders at low Reynolds number †

Shun Chang Yen* and Chien Ting Liu

Department of Mechanical and Mechatronic Engineering, National Taiwan Ocean University, Keelung, Taiwan 202, R.O.C.

(Manuscript Received March 6, 2011; Revised June 28, 2011; Accepted July 22, 2011)

Abstract

The flow structures, drag coefficients (C_d) and vortex shedding characteristics around a single square cylinder and twin side-by-side square cylinders were experimentally investigated with various Reynolds numbers (*Re*) and gap ratios (g*) in a vertical water tunnel. The Reynolds number (*Re*) and gap ratio (g*) were $178 < Re < 892$ and $0 \le g^* \le 2.5$, respectively. The flow patterns and vortex shedding frequency were determined using the particle tracking flow visualization (PTFV). The flow structures, velocity properties, and drag coefficients were calculated using the particle image velocimetry (PIV). The topological flow patterns of vortex evolution processes were plotted and analyzed based on critical point theory. Furthermore, the flow structures behind twin side-by-side square cylinders were classified into three modes — *single vortex-street mode*, *gap-flow mode* and *couple vortex-streets mode*. The maximum C_d occurred in the single vortex-street mode, and the minimum C_d occurred in the gap-flow mode. The highest Strouhal number (*St*) occurred in the single vortex-street mode, and the lowest *St* occurred in the gap-flow mode.

Keywords: Twin-cylinders; PTFV; PIV; Gap flow

---

1. Introduction

The bluff-body flows have attracted considerable interest and have been extensively studied for the application of the low–pressure recirculation zone and vortex-shedding behaviors. Many bluff bodies with various cross sections were commonly utilized in the architectural structures such as skyscrapers, bridge decks, monuments, and other buildings. Specifically, these structures are installed in various arrangements to accommodate the space constraints or other architectural considerations. Zdravkovich [1] and Ishigai and Nishikawa [2] investigated the gap flow between circular cylinders in single-column, single-row, and double-row cylinder arrangements. The flow interference depends on the spacing between the cylinders and the orientation relative to the free stream. Three categories of flow interference were proposed — proximity interference, wake interference and a combination of both categories. Moreover, the flow structure, vortex formation and force coefficient were discussed.

Many studies concentrated on the flow patterns around and behind the single-cylinder and two-cylinder configurations. Zdravkovich [3] examined the interference of flow fields for one, two tandem, and two side-by-side circular cylinders. The flow patterns, lift-to-drag ratios, surface-pressure distributions, velocity profiles, and vortex-shedding behaviors were investigated for various cylinder arrangements. The wake-flow patterns behind a circular cylinder with different *Re* were classified as laminar-separation or separation-bubble modes. The wake-flow patterns behind two tandem circular cylinders with different spacing ratios were also classified as single slender-body, reattachment, or binary vortex-street modes. The wake-flow patterns behind two side-by-side circular cylinders were classified as single-vortex street, biased gap-flow, or coupled vortex-street modes by using various gap ratios. Williamson [4] used several flow-visualization methods to examine the flow field behind two side-by-side circular cylinders. Williamson found that the vortex shedding synchronized at $1.0 < g^* < 5.0$, where g* is the gap ratio of the spacing between the cylinder surfaces relative to the cylinder diameter. This synchronization generated two parallel vortex streets in phase and in anti-phase. When $g^* < 1.0$, a harmonic vortex-shedding modes existed behind the cylinders. Alam et al. [5] determined the wake characteristics, switching phenomena and characteristics of aerodynamic loadings acting on two circular cylinders placed in side-by-side arrangement. They found that two major flow regimes characterized by the wake-flow behavior were distinguished using various spacing between two side-by-side circular cylinders. The fluid forces separated the modes into wide wake mode and narrow wake mode in the bistable flow regime.

† This paper was recommended for publication in revised form by Associate Editor Simon Song
*Corresponding author. Tel.: +886 2 2462 2192, 3215, Fax.: +886 2 2462 0836
E-mail address: scyen@mail.ntou.edu.tw

Additionally, many numerical studies and experimental researches investigate the flow behavior around a square cylinder. Kolar et al. [6] used a laser Doppler velocimeter (LDV) to detect the average flow behavior around/behind two side-by-side, identical square cylinders while *Re* is approximately 23,100. Kolar et al. indicated that the enhanced vortex motion and the average vortex speed in the base region were significantly high, even in the eventual near-wake equilibrium state (i.e., low vortex-speed state). Furthermore, the Strouhal number (*St*) behind two side-by-side, identical square cylinders is slightly higher than that behind the single square cylinder. Wong et al. [7] carried out the experiments in a low-speed wind tunnel with a test section of 56 cm × 56 cm. They tested the aerodynamic forces and vortex shedding of two square cylinders in a side-by-side arrangement with a dimension ratio of 2:1 in a subcritical flow regime. The gap-side shear layer on the large cylinder reattached to its inner face conducted a small separation, while the gap-side shear layer of small cylinder reattached to its inner face conducted a large separation. Moreover, the distributions of aerodynamic forces revealed that the maximum pressure on the small cylinder occurred at $g^* = 1.75$. In theoretical studies, Inoue et al. [8] utilized the finite difference method to solve a two-dimensional (2D) unsteady compressible Navier-Stokes equation for two square cylinders placed in a side-by-side arrangement. They found that the flow field depended on the gap spacing; and furthermore, they identified six wake patterns as non-synchronized, anti-phase and in-phase synchronized, flip-flopping, single bluff-body and steady modes.

The main purpose of the current study is to investigate the characteristic flow patterns and surface-flow behaviors around/behind two identical side-by-side square cylinders at low Reynolds numbers. The effects of Reynolds number ($178 < Re < 892$) and gap spacing ($0 \le g^* \le 2.5$) between two square cylinders were examined. The flow patterns were investigated using the particle tracking flow visualization (PTFV). Experimental data were measured and analyzed by using particle image velocimetry (PIV). Furthermore, the experimental data were applied to calculate the velocity distributions, drag coefficients, and vortex-shedding frequencies. The objectives of this study are listed as follows: (1) to elucidate the interaction between the twin square cylinders; (2) to evaluate the drag coefficients; and (3) to detect the vortex shedding frequency.

2. Experimental arrangements

2.1 Experimental setup

Fig. 1 depicts the experimental setup utilized in this study which was adopted in Yen et al. [9]. The experiments were conducted in a vertical water tunnel. The test section was 30 cm deep, 30 cm wide, and 90 cm high. The free-stream turbulence intensity was approximately 0.5% in a velocity range of 0.5-6 cm/s. Water was stored in a stainless steel tank and driven by a centrifugal pump. The water flowed through the

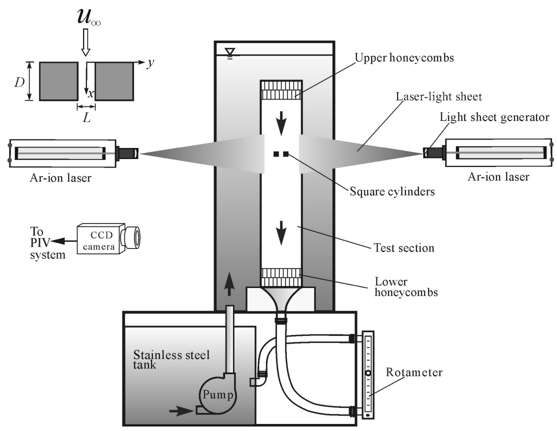

Fig. 1. Experimental setup.

upper honeycombs, square cylinders, lower honeycombs, and rotameters and then returned to the stainless tank. The dimensions of hexagonal honeycomb in this study were 0.65 cm in length and 6 cm in height. The dimensions of the upper honeycombs were 30 × 30 × 6 cm in depth, width and height, respectively. The dimensions of external water tank were 60 × 60 × 106 cm^3 in depth, width and height, respectively. Rotameters were utilized to determine the flow rate, and the reading error was calibrated within ±2%.

The square cylinders were manufactured from acrylic bars and supported by stainless steel rods. The dimensions of the square cylinders were 30 cm × 2 cm × 2 cm (depth × width × height). Therefore, the aspect ratio (*AR*) and blockage ration (*BR*) were 15 and 13% by referencing the results of Mittal [10], Lam and Zou [11], and West and Apelt [12]. For visualizing the flow field, the PIV scheme was utilized and set up as shown in Fig. 1. Fig. 1 delineates that the *x*-axis was parallel to the flow direction, the *y*-axis was perpendicular to the flow direction, and the *z*-axis was perpendicular to the *x* and *y* axes. Specifically, the laser beam was focused on the mid-plane of the acrylic bars. In this investigation, the distance between the focused mid-plane and test-section wall is 7.5D. Consequently, the end-wall effect is neglected (Lam and Zou [11], West and Apelt [12]).

In the PIV and PTFV systems, the polyamide (PM) particles were seeded in the water tunnel to scatter laser light, and the PM particles had a diameter range of 35–70 μm. The laser wavelength was 540 nm, and the reflectivity of the PM particles was 1.59. The relaxation time constant was estimated to be $< 6.25\times10^{-5}$ sec, and the Stokes number was on the order of 10^{-6}. Therefore, the effect of turbulent diffusion was neglected, and the slip between the water flow and PM particles was negligible. The maximum fluctuation frequency of PM particles was estimated to be 3 kHz according to the method developed by Mei [13].

2.2 PIV measurements

The PIV image-acquisition system included two argon-ion lasers, a CCD camera, and a data-translation board (Fig. 1). A cross-correlation-based PIV utilizing the single exposed double frame images was applied to visualize the flow structures. The laser-light sheet was 0.6 mm thick and was adjusted by a 20-degree laser-light-sheet expander. The lasers were Spectra-Physics' Stabilite-2017 6-Watt argon-ion lasers, and the laser light was transmitted through an optical fiber. The particle images were recorded using a CCD camera (Redlake MASD, Inc. Model MotionScope PCI 2000S) with a resolution of 480 × 420 pixels. The field of view was approximately 10 cm × 10 cm, which corresponded to a spatial resolution of about 208 μm/pixel. The maximum frame rate was 2,000 frames/s (fps), and the exposure time was 0.025–20 μs. The Data Translation board (MotionScope PCI controller) was adopted to digitize the analog voltage output from the CCD camera.

The PIV post-processing system was composed of an image interrogation and a post interrogation system. Two consecutive image frames were analyzed using the cross-correlation technique [14]. This technique was embedded in the software VidPIV4, which was obtained from Optical Flow Systems. The software calculated the average displacement of local particle groups in the consecutive images. The interrogation window was set to 32 × 32 pixels. In order to reduce the velocity bias in the regions with large velocity gradients, the ratio of the displacement of single exposed double frame images in the length of the interrogation area was maintained at a value smaller than 1/4, as suggested by Keane and Adrian [15]. Filtering and interpolation were used to identify outliers and to regenerate the missed values. The global filter found all the globally inconsistent values, whereas the local filter found values that may be globally consistent but are not smoothly consistent with the local variations in vector magnitude and direction. This method of interpolation was based on a weighted mean technique that replaced the values at filtered sites in an iterative manner by replacing those values with the greatest number of surrounding valid values first and working toward values that were less favorably positioned. Adaptive cross-correlation, a smaller interrogation size, and smaller grid spacing were applied to the vector field generated from the regular procedures for cross correlation, filtering (global and local), and interpolation in order to provide higher resolution and accuracy than the first pass. The interpolation process was based on the weighted mean method and was used to calculate the ensemble average velocity. Instantaneous vector fields were utilized to obtain the mean velocity.

The uncertainty (U) estimated in the measurements was based on the method of Abernethy et al. [16]. The uncertainty, with a 95% confidence level, was derived as follows:

$$U = \left[B^2 + \left(t S_{\bar{x}} \right)^2 \right]^{1/2} \tag{1}$$

where B is the bias error, $S_{\bar{x}}$ is the precision index of the average, and t is the Student's distribution. For large samples, $t = 2$ in Eq. (1). The bias error was estimated from the calibrated data and previous experimental judgment. The precision index of the average was computed from the random error of the measured data. Hence, the uncertainty in the velocity measurements was approximately 4.8% in this study.

2.3 Flow visualization

In this study, the long-exposed particle trajectories visualized using the particle-tracking flow method were recorded by a Nikon Model D70s camera (Resolution = 3,008 × 2,000 pixels, exposure time = 30-1/8,000s). The particle tracking flow visualization was illuminated by a 0.6 mm-thick laser-light sheet adjusted with a 20-degree laser-light-sheet expander. A square cylinder with a width of 2 cm (with a cross section that was 2 cm × 2 cm) was towed at 1-5 cm/s. Experimentally, the vortex shedding frequency was obtained using continuous images stored in a computer. These continuous images were recorded by using a Redlake MotionScope PCI 2000S CCD camera with an exposure time of 1/250 sec and a framing rate of 250 fps. Identification, analysis of formation, and vortex evolution processes behind the square cylinder were conducted by replaying the movies of the particle images on a computer monitor. The vortex shedding frequency was detected from 1.14 to 8.9 Hz using different gap ratios and flow speeds. Therefore, the characteristic time scale of the large eddies was in the range of 0.112-0.877 sec. The shutter speed and the framing rate were set at 1/250 sec and 250 frames/s, respectively. Consequently, the uncertainty of the vortex shedding frequency was approximately ±3.3%.

3. Results and discussion

3.1 Flow patterns based on particle tracking and characteristic flow modes

The particle tracking flow visualization includes the fluorescent particles and laser light sheet illumination (Adrian [17]). The pathlines of fluorescent particles were recorded on the streak films with long exposure times and low framing rates. The exposed particle trajectories were delineated using numerous pathline segments. Additionally, the turbulence intensity was varied by the Reynolds number (Re) and the gap ratio as water moved around the square cylinders. The Reynolds number was defined as $Re = \rho u_\infty D/\mu$, where ρ is the water density, u_∞ is the free-stream velocity, D is the square width, and μ is the dynamics viscosity of water. The gap ratio was defined as $g^* = L/D$, where L represents the spacing between these two cylinder surfaces. Furthermore, the gap ratio was adjusted from 0 to 2.5 in this investigation.

Fig. 2 shows the particle tracking flow patterns behind the square cylinders at $Re = 357$ and an exposure time = 0.75 sec. The typical flow pattern behind a single square cylinder, shown in Fig. 2(a), was similar to the pattern obtained by Okajima [18] and Bearman and Trueman [19]. In Fig. 2(a), the flow separated at the leading edges, and a four-way saddle appeared at (x/D, y/D) ≈ (2.6, 0) to form an envelope in the

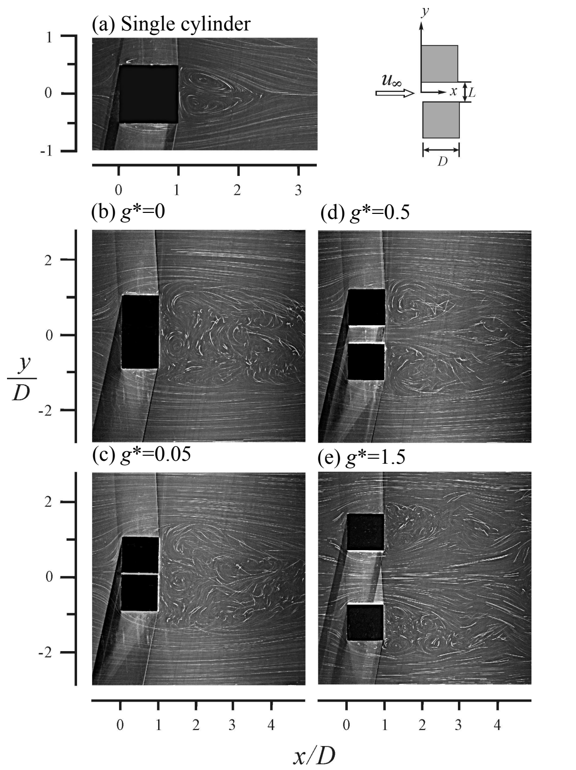

Fig. 2. Photos of the streak flow patterns at Re = 357; exposure time = 0.75 sec.

wake. No reattachment occurred on the lateral surfaces of the cylinder, and two similar stable recirculations were observed behind the cylinders.

In Fig. 2(b), two identical square cylinders were side-by-side together (g* = 0) to form a rectangular bulk. The flow separated from the two leading edges of the bulk, and a pair of recirculations was observed in the wake. No reattachment occurred on the lateral surfaces. The flow pattern was analogous to the pattern displayed in Fig. 2(a). However, the flow structure was more turbulent than the structure developed in the single-cylinder case because a large low-pressure region formed behind the rectangular bulk. Fig. 2(c), where g* = 0.05, displays a flow structure similar to the structure shown in Fig. 2(b). This flow pattern was called *single vortex street mode* due to the low gap ratios.

In Fig. 2(d), where g* = 0.5, the jet flow moves through the opening between the two identical cylinders. The flow between these two square cylinders was constrained due to the low gap ratio. Therefore, no separation occurred on the inner cylinder surfaces. For g*= 0.1 to 1.0 (i.e., in the gap-flow mode), the constrain effect on the gap flow decreased as the g* increased. Moreover, the jet flow behind the square cylinders could not maintain its initial discharge direction and was biased in alternate directions by the Coanda effect (Coanda [20] and Newman [21]). Therefore, two recirculations with different rotation directions appeared behind each cylinder. The flow structure exhibits anti-phase vortex shedding (Yen and Liu [22]). This flow pattern was called the *gap flow mode*.

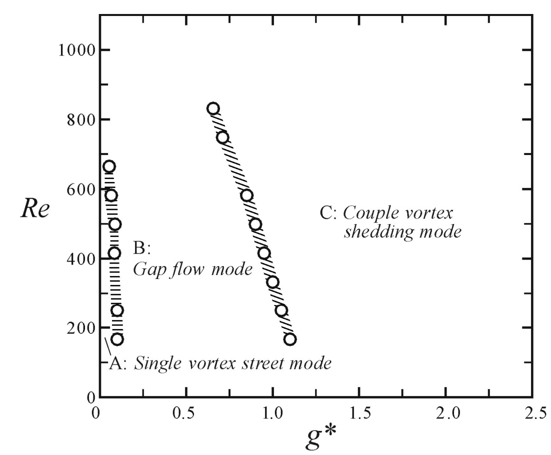

Fig. 3. Distribution of characteristic flow modes.

Fig. 2(e) illustrates the flow patterns behind the cylinders for a large gap ratio such as g* = 1.5. The flow structure shows that two anti-phase vortex shedding events occurred behind each cylinder. Two pairs of opposite-direction vortices were observed in the wake due to the gap flow effect. This flow pattern was called the *couple vortex streets mode*.

Fig. 3 depicts the regimes of the characteristic flow patterns in relation to g* and Re. The particle tracking flow patterns were used to classify the wake flow into three modes: *single vortex street mode*, *gap flow mode*, and *couple vortex streets mode*. The effect of Re on the flow patterns is insignificant for low g*. This low Re-effect on the flow structures was also found by Yen and Liu [22]. However, in the gap-flow mode at low Re, the viscous effect on the flow patterns is notable. Namely, the flow direction was biased by the Coanda effect. The borders that separated different characteristic flow regimes had some uncertainties. The maximum uncertainties were ±0.1 for g* and ±20 for Re.

3.2 Streamline patterns and vorticity contours

The ensemble-average streamline patterns and vorticity contours of the flow fields were quantitatively determined using the single exposed double frame images recorded from the cross-correlation-based PIV measurement. Figs. 4 and 5 display the ensemble-average streamline patterns and vorticity contours by changing the gap ratio at Re = 357.

Streamline Patterns. Fig. 4 shows the ensemble-average evolution process of streamline patterns derived from the vector plots and the lost signals that were amended using the shooting method. Additionally, Fig. 4 indicates the sequence of vortex motions and the coordinates with the streak patterns (Fig. 2). In Fig. 4(a), for a single square cylinder, a saddle point is located at (x/D, y/D) ≈ (2.6, -0.2), and a pair of recirculation nodes is located at (x/D, y/D) ≈ (1.4, ± 0.4). The flow structure was similar to that displayed in Fig. 2(a). In Fig. 4(b), where g* = 0, a pair of recirculation nodes was located at (x/D,

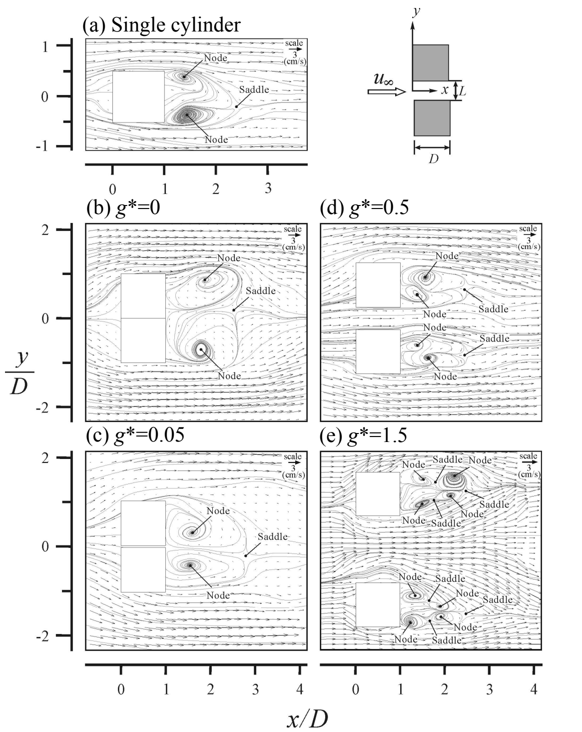

Fig. 4. Velocity vector fields and streamline patterns at Re = 357: (a) a single square cylinder model; (b) single vortex street mode, g^* = 0; (c) single vortex street mode, g^* = 0.05; (d) gap flow mode, g^* = 0.5; (e) couple vortex streets mode, g^* = 1.5.

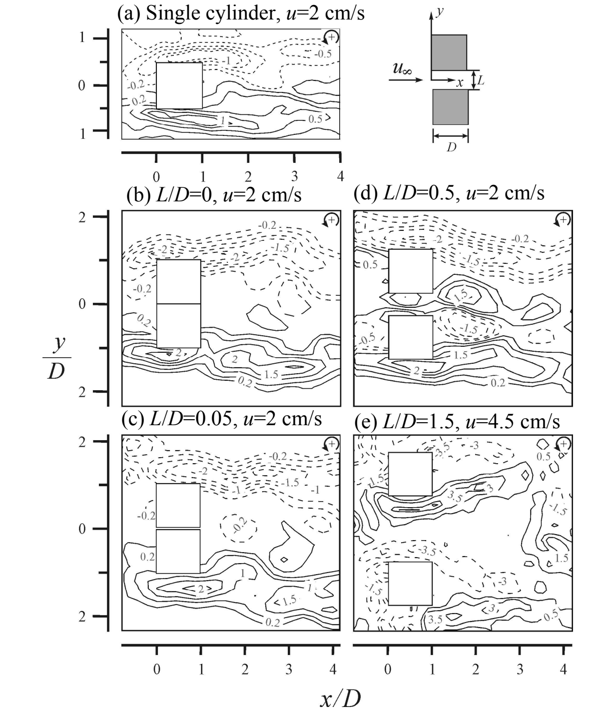

Fig. 5. Vorticity contours at Re = 357: (a) a single square cylinder model; (b) single vortex street mode, g^* = 0; (c) single vortex street mode, g^* = 0.05; (d) gap flow mode, g^* = 0.5; (e) couple vortex streets mode, g^* = 1.5. The solid and dashed lines represent the positive and negative vorticity magnitude.

y/D) ≈ (1.8, ±1.75), and an off-axis saddle point was located at (x/D, y/D) ≈ (2.6, 0.15). The flow structure was similar to the *single vortex street mode* as shown in Fig. 2(b). Similarly, Fig. 4(c) presents a saddle point at (x/D, y/D) ≈ (2.8, -0.5) and a pair of recirculation nodes at (x/D, y/D) ≈ (1.6, ±0.35) when g^* = 0.05. The flow structure in Fig. 4(c) was similar to the *single vortex street mode* visualized in Fig. 2(c).

In Fig. 4(d), in which g^* = 0.5, the jet flow moves through the gap between the two identical cylinders. No separation occurred on the cylinder surfaces, and a pair of recirculations appeared behind each cylinder. Moreover, two saddle points were present at (x/D, y/D) ≈ (2.4, 0.75) and (2.4, -0.9), and four recirculation nodes were found at (x/D, y/D) ≈ (1.5, ±0.6) and (1.75, ±1.0). This flow structure was similar to the gap flow mode that was displayed in Fig. 2(d). In Fig. 4(e), g^* = 1.5, and six off-axis saddle points as well as eight nodes were present behind the cylinders. This flow structure was similar to the *couple vortex streets mode* as demonstrated in Fig. 2(e).

***Vorticity Contours*:** The vorticity (Ω_z) is determined using the mean velocity distribution and the definition of vorticity is listed as follows:

$$\Omega_z = \frac{\partial v}{\partial x} - \frac{\partial u}{\partial y} \tag{2}$$

where u and v denote the x- and y-component velocities, respectively. The counterclockwise rotation yields the positive vorticity defined in this investigation. Moreover, Fig. 5 plots the distribution of ensemble-average vorticity and the local maximum vorticities occurs at the nodes and saddle points.

Fig. 5(a) presents the distribution of vorticity for a typical flow around a square cylinder. In Fig. 5(a), two mirrored vortices with the highest vorticity were found in the wake where a clockwise (negative) vortex was present in the upper-right corner of this panel, and a counterclockwise (positive) vortex was observed in the lower-right region. Figs. 5(b) and (c) show the vorticity contour of the *single vortex street mode*. The vortices formed in the upper region of these panels moved clockwise (negatively), while the vortices located in the lower region rotated counterclockwise (positively). Fig. 5(d) displays the vorticity contour in the *gap flow mode* where two pairs of mirrored vortices with the highest vorticity formed behind the cylinders. Fig. 5(e) shows the vorticity distributions of the *couple vortex streets mode*. Four pairs of mirrored vortices with the relatively high vorticity formed in the wake.

3.3 Topological analysis

Lighthill [23], Perry and Fairlie [24], and Chong and Perry [25] utilized topology to analyze the flow field. Specifically, Perry and Steiner [26] adopted the critical point theory to define the nodes (foci or centers included), saddles, bifurcation lines, separatrices, critical points, and alleyways. The topological analysis explicates the flow structures of the steady flow or the unsteady wake-flow evolution. Moreover, many singular points occur at some particular positions where the velocity is zero and the streamline slope is indeterminate when the flow moves around a three-dimensional bulk (Madeleine and Gerard [27]). Specifically, the nodal point presents either flow attachment or flow separation. At the node of flow attachment, all of the topological lines direct outward away from this node. However, at the node of flow separation, the topological lines direct inward (that is, point away from the node). The saddle point occurs at the intersection of two topological lines (Josef [28]). Furthermore, the half-nodes and half-saddles occur on the two-dimensional plane cut through a three-dimensional body. Collectively, Hunt et al. [29] utilized the topological analysis to formulate the relationship between the nodes, saddles and entities in the flow field. The topological relationship is listed as follows:

$$\left(\sum N+\frac{1}{2}\sum N'\right)-\left(\sum S+\frac{1}{2}\sum S'\right)=1-n \quad (3)$$

where N, N', S and S' represent the four-way node, three-way node, four-way saddle and three-way saddle, respectively, and n is the connectivity of the considered flow section.

Fig. 6 displays the topological flow structures, which were determined from the flow patterns (Figs. 2, 4, and 5). Fig. 6(a), for a single square cylinder, depicts two nodes (N_1 and N_2), one off-axis four-way saddle (S_1), four three-way saddles (S_1', S_2', S_3' and S_4'), and n = 2 when one object was installed in the flow field. The critical points in Fig. 6(a) are $\sum N = 2$, $\sum N' = 0$, $\sum S = 1$ and $\sum S' = 4$. Therefore, these values fulfilled the topological condition (Eq. (3)). Fig. 6(b), for the single vortex street mode, shows that the critical points, $\sum N = 2$, $\sum N' = 0$, $\sum S = 1$, $\sum S' = 4$ and $n = 2$, also satisfied the topological rule. Fig. 6(c) depicts the topological flow pattern of the gap flow mode where the critical points are $\sum N = 4$, $\sum N' = 0$, $\sum S = 2$ and $\sum S' = 8$. In the gap flow patterns, $n = 3$ because two square cylinders were present. The topological flow mode shown in Fig. 6(d) is the couple vortex streets mode where the critical points, $\sum N = 8$, $\sum N' = 0$, $\sum S = 6$ and $\sum S' = 8$ were consistent with Eq. (3).

3.4 Drag coefficients

In this section, the drag coefficient of the twin side-by-side square cylinders was tested and analyzed based on the mean streamwise velocity profiles obtained from the ensemble average scheme.

Velocity Profiles: Fig. 7 plots the streamwise velocity distributions at x/D = -3.0, -1.3, -0.7, -0.1, 1.1, 1.7, 2.5, 2.7, 2.8, 3.7, 4.3, and 5.0 at Re = 357 by using the ensemble average velocity profiles (frame rate = 250 fps). The velocity near y/D = 0 declined from x/D = -1.8 to -0.1 and then increased down-

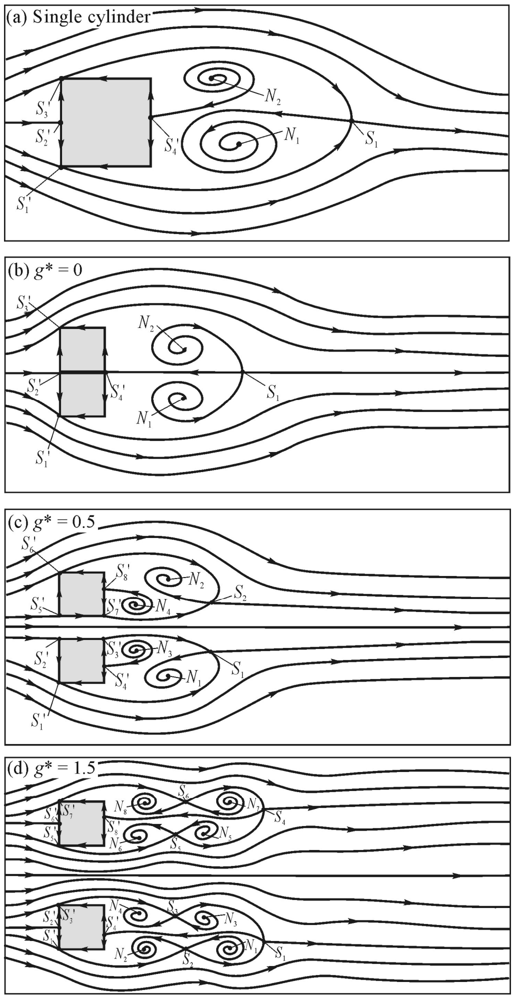

Fig. 6. Proposed topological flow structures: (a) a single square cylinder model; (b) single vortex street mode, g^* = 0; (c) gap flow mode, g^* = 0.5; (e) couple vortex streets mode, g^* = 1.5.

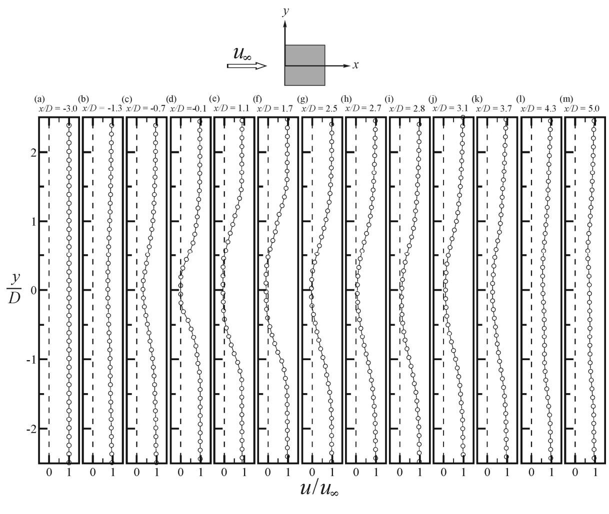

Fig. 7. Normalized velocity distributions at x/D: (a) -3.0; (b) -1.3; (c) -0.7; (d) -0.1; (e) 1.1; (f) 1.7; (g) 2.5; (h) 2.7; (i) 2.8; (j) 3.7; (k) 4.3; (l) 5.0 of the single square cylinder model at Re = 357.

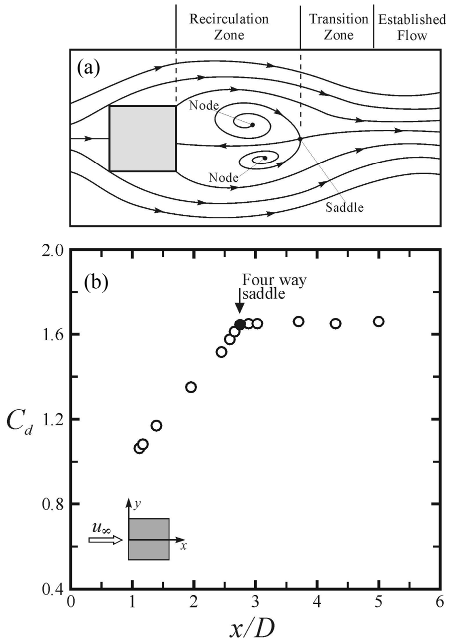

Fig. 8. (a) Topological flow system behind a single square cylinder; (b) Drag coefficient with respect to *x/D* at *Re* = 357.

stream. Fig. 7(a) indicates that the freestream velocity was not disturbed in the upstream. Fig. 7(c) presents a stagnation point close to the origin of the *x*-*y* plane. In Fig. 7(d), at *x/D* = 1.1, the negative velocities near *y*/*D* = 0 revealed that the reverse flow appeared behind the cylinder. Reverse flow was also observed in Fig. 4(a). Fig. 7(g) shows a zero-speed point at (*x/D*, *y*/*D*) = (2.7, 0), which can also be observed in Fig. 4(a).

Drag Coefficients: Fig. 8(a) presents the flow fields behind a single square cylinder. The drag coefficient (C_d) was calculated from the velocity fields (shown in Fig. 7) by using the results presented by Unal et al. [30] The drag was applied when the integration plane was taken sufficiently far downstream of the model so that the pressure had recovered to its undisturbed value. Fig. 8(b) plots the distribution of the drag coefficient with respect to *x/D* for a single square cylinder at *Re* = 357. The drag coefficient increased with *x/D* and approached a constant when *x/D* > 2.7 where a four-way saddle point occurred.

Fig. 9 plots the profile of C_d against *Re*. The velocity distribution for calculating C_d was located at the four-way saddle point determined by using the method in Fig. 8. The value of C_d (void circle) for a single square cylinder model was consistent with the results (solid circle) of Okajima [31]. For two contact square cylinders (g^* = 0), C_d exceeded the that for a single square cylinder model. Moreover, C_d = 2.06 while *Re* = 178, which was consistent with that of C_d = 2.01 obtained by Sohankar et al. [32]. The relationship between C_d and the width/height ratio was also consistent with those found by Sohankar et al. [32]. The drag coefficient in the single vortex-street mode (g^* = 0) exceeded those from other flow modes

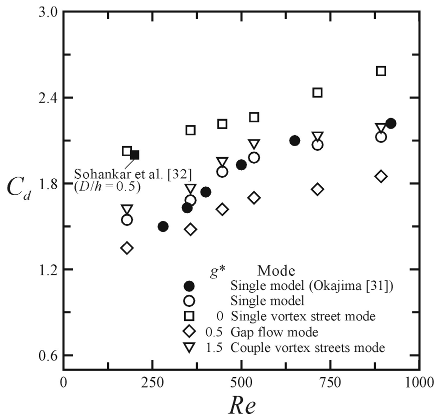

Fig. 9. Drag coefficient against Reynolds number.

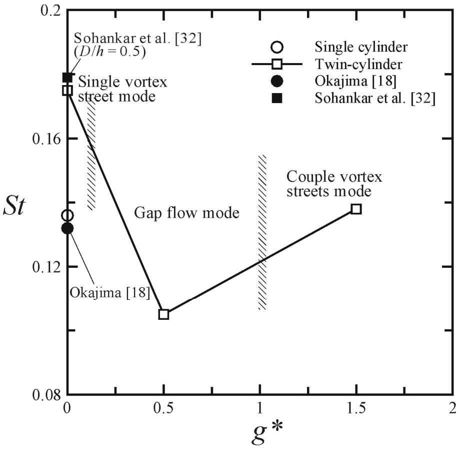

Fig. 10. Variation of Strouhal number versus gap ration while *Re* = 357.

and approached that for a single square cylinder model as g^* > 1.5 (i.e., in the couple vortex-streets mode). The lowest C_d occurred in the gap-flow mode, and the highest C_d occurred in the single vortex-street mode.

3.5 Vortex-shedding frequency

The vortex-shedding frequency (*f*) behind the cylinders varied with the gap ratio while *Re* = 357. The relationship between the vortex-shedding frequency and gap ratio was examined for various Strouhal numbers ($St = fD/u_\infty$). Fig. 10 displays the variation of *St* against g^* behind a single square cylinder and twin side-by-side square cylinders while *Re* = 357. The data point (void circle) is similar to that (solid circle) obtained by Okajima [18] for a single square cylinder. At g^* = 0, the Strouhal number was approximately 0.176, which was close to *St* = 0.179 obtained by Sohankar et al. [32]. In this investigation the highest *St* of 0.176 occurs in the single vortex-street mode. The flow separates from the two outer leading vertices of the rectangle-like bulk, and a pair of recirculation occurs in the wake. No reattachment occurs on the lateral square-cylinder surfaces. Furthermore, the relatively wide low-pressure zone causes the maximum C_d (2.17). In the gap-flow mode, the lowest *St* of 0.12 and minimum C_d of 1.48 occurs at $g^* = 0.5$. In the couple vortex streets mode, the *St* of o.138 and C_d of 1.68 are approximately equal to that of a single-square cylinder model.

4. Conclusions

The characteristics of flow around square cylinders at various Reynolds numbers and gap ratios were examined. The behaviors and flow patterns were studied using particle tracking flow visualization (PTFV). Flow structures, velocity distributions, drag coefficients, characteristics and shedding frequencies were determined with a particle image velocimetry (PIV) scheme. The experimental results and discussion support the following conclusions.

By changing *Re* and *g**, the flow field was categorized into three distinct modes: *single votex street mode, gap flow mode, and couple vortex streets mode*.

The lowest drag coefficient occurred in the gap-flow mode, and the highest drag coefficient occurred in the single vortex-street mode.

The lowest *St* occurred in the gap-flow mode, and the highest *St* occurred in the single vortex-street mode.

Acknowledgment

This research was supported by the National Science Council of the Republic of China, under Grant No. NSC 97-2221-E-019-039.

Nomenclature

AR	: Aspect ratio of square (= depth length/ width length)
BR	: Blockage ratio (= model area/ test section area)
C_d	: Drag coefficient
D	: Square width, 2 cm
f	: Vortex shedding frequency (Hz)
*g**	: Gap ratio (= *L/D*)
L	: Gap spacing between two cylinder surfaces (cm)
Re	: Reynolds number (= $u_\infty D/\nu$)
St	: Strouhal number (= $f D/ u_\infty$)
u_∞	: Free stream velocity
u	: The *x*-component of local instantaneous velocity
x	: Streamwise coordinate
y	: Spanwise coordinate
μ	: Dynamics viscosity of water
ρ	: Density of water
v	: Kinetic viscosity of water

References

[1] M. M. Zdravkovich, Review of flow interference between two circular cylinders in various arrangements, *ASME Journal of Fluids Engineering*, 99 (1977) 618-633.

[2] S. Ishigal and E. Nishikawa, Experimental study of structure of gas flow in tube banks with tube axes normal to flow (Part II, On the structure of gas flow in single-column, single-row, and double-row tube banks), *Bulletin of the JSME*, 18 (1975) 528-535.

[3] M. M. Zdravkovich, Flow around Circular Cylinders: A Comprehensive Guide through Flow Phenomena, *Experiments, Applications, Mathematical Models, and Computer Simulations*, Vol. 1: Fundamentals. Oxford University Press, New York, USA (1997).

[4] C. H. K. Williamson, Evolution of a single wake behind a pair of bluff bodies, *J. Fluid Mech.*, 159 (1985) 1-18.

[5] M. M. Alam, M. Moriya and H. Sakamoto, Aerodynamic characteristics of two side-by-side circular cylinders and application of wavelet analysis on the switching phenomenon, *Journal of Fluids and Structures*, 18 (2003) 325-346.

[6] V. Kolar, D. A. Lyn and W. Rodi, Ensemble-average measurements in the turbulent near wake of the two side-by-side square cylinders, *J. Fluid Mech.*, 346 (1997) 201-237.

[7] P. T. Y. Wong, N. W. M. Ko and A. Y. W. Chiu, Flow characteristics around two parallel adjacent square cylinders of different sizes, *Journal of Wind Engineering and Industrial Aerodynamics*, 54/55 (1995) 263-275.

[8] O. Inoue, W. Iwakami and N. Hatakeyama, Aeolian tones radiated from flow past two square cylinders in a side-by-side arrangement, *Phys. Fluids*, 18 (2006) 046104.

[9] S. C. Yen, K. C. San and T. H. Chuang, Interactions of tandem square cylinders at low Reynolds numbers, *Experimental Thermal and Fluid Science* 32 (2008) 927-938.

[10] S. Mittal, Computation of three-dimensional flows past circular cylinder of low aspect ratio, *Physics of Fluids,* 13 (2001) 177-191.

[11] K. Lam and L. Zou, Three-dimensional numerical simulations of cross-flow around four cylinders in an in-line square configuration, *Journal of Fluids and Structures,* 26 (2010) 482-502.

[12] G. S. West and C. J. Apelt, The effects of tunnel blockage and aspect ration on the mean flow past a circular cylinder with Reynolds number between 10^4 and 10^5, *Journal of Fluid Mechanic*, 114 (1982) 361-377.

[13] R. Mei, Velocity fidelity of flow tracer particles, *Exp. Fluids*, 22 (1) (1996) 1-13.

[14]R. D. Keane and R. J. Adrian, Theory of cross-correlation analysis of PIV images, *Applied Scientific Research*, 49 (2) (1992) 191-215.

[15] R. D. Keane and R. J. Adrian, Optimization of particle image velocimeters (Part I: Double pulsed systems), *Measurement Science and Technology*, 1 (11) (1990) 1202-1215.

[16] R. B. Abernethy, R. P. Benedict and R. B. Dowdell, ASME measurement uncertainty, *ASME Journal of Fluids Engineering*, 107 (2) (1985) 161-164.

[17] R. J. Adrian, *Laser Velocimetry, Fluid Mechanics Measurements,* 2nd ed., Ed. Goldstein, R. J., Taylor & Francis, Washington DC (1996) 175-299.

[18] A. Okajima, Strouhal numbers of rectangular cylinders, *J.*

Fluid Mech., 123 (1982) 379-398.
[19] P. B. Bearman and D. M. Trueman, An investigation of the flow around rectangular cylinders, *Aero. Quart*, 23 (1972) 229-237.
[20] H. Coanda, Device for deflecting a stream of elastic fluid projected into an elastic fluid, *United States Patent Office* (1936) 2052869.
[21] B. G. Newman, The deflection of plane jets by adjacent boundaries–Coanda effect, *Boundary Layer and Flow Control: Its Principles and Application*, Vol. 1, Ed. Lachmann, G. V., Pergamon Press, New York (1961) 232-264.
[22] S. C. Yen and J. H. Liu, Wake flow behind two side-by-side square cylinders, *International Journal of Heat and Fluid Flow,* 32 (2011) 41-51.
[23] M. J. Lighthill, *Laminar Boundary Layers*, Oxford University Press, Cambridge (1963) 48-88.
[24] A. E. Perry and B. D. Fairlie, Critical points in flow patterns, *Advances in Geophysics B*, 18 (1974) 299-315.
[25] M. S. Chong and A. E. A. Perry, General classification of three-dimensional flow fields, *Physics of Fluids A*, 2 (5) (1990) 765-777.
[26] A. E. Perry and T. R. Steiner, Large-scale vortex structures in turbulent wakes behind bluff bodies (Part 1. Vortex formation), *J. Fluid Mech.*, 174 (1) (1987) 233-270.
[27] C. Madeleine and P. Gerard, Some type mechanisms in the early phase of the vortex-shedding process from particle-streak visualization, *Atlas of Visualization*, Vol. III, Ed. Y. Nakagama and Y. Tanida, CRC Press, Boca Raton (1997) 43.
[28] R. Josef, The topology of separating and reattaching vortical flows, *High Angle of Attack Aerodynamics: Subsonic, Transonic, and Supersonic Flows*, Springer-Verlag, New York, USA (1992) 62.
[29] J. C. R. Hunt, C. J. Abell, J. A. Peterka and H. Woo, Kinematical studies of the flows around free or surface-mounted obstacles; applying topology to flow visualization, *J. Fluid Mech.*, 86 (1) (1978) 179-200.
[30] M. F. Unal, J. C. Lin and D. Rockwell, Force prediction by PIV imaging: A momentum based approach, *J. Fluids Struct.*, 11 (1997) 965-971.
[31] A. Okajima, Numerical analysis of the flow around an oscillating cylinder, *Proceedings of the 6th International Conference on Flow-Induced Vibration*, Ed. Bearmen, P. W., London, UK, Balkema, Rotterdam (1995) 1-7.
[32] A. Sohankar, C. Norberg and L. Davidson, Numerical simulation of unsteady flow around a rectangular two-dimensional cylinder at incidence, *Journal of Wind Engineering and Industrial Aerodynamics*, 69 (1997) 189201.

Shun Chang Yen, Associate Professor of Mechanical and Mechatronic Engineering Department in National Taiwan Ocean University, Taiwan, received his B.S. degree from Chinese Air Force Academy in 1992 and Mechanical Engineering M.S./Ph.D of National Taiwan University of Science and Technology, Taiwan in 1998 and 2003. His researches cover fluid mechanics, aerodynamics, combustion technology, chemically reacting flows and related fields.